Postprint of: Wołoszyk K., Bielski P., Garbatov Y., Mikulski T., Photogrammetry image-based approach for imperfect structure modelling and FE analysis, OCEAN ENGINEERING, Vol. 223 (2021), 108665, DOI: 10.1016/j.oceaneng.2021.108665

Photogrammetry image-based approach for imperfect structure modelling and FE analysis

Krzysztof Woloszyk[a], Pawel Michal Bielski[a], Yordan Garbatov[b, 1], Tomasz Mikulski[a]

[a] *Institute of Naval Architecture and Ocean Engineering, Gdansk University of Technology, G. Narutowicza 11/12 st., 80-233 Gdansk, Poland*

[b] *Centre for Marine Technology and Ocean Engineering (CENTEC), Instituto Superior Técnico, Universidade de Lisboa, Avenida Rovisco Pais 1049-001 Lisboa, Portugal*

Abstract

This study aims to model and analyse imperfect structures using real measurements, employing photogrammetry technique commonly used in the geodesy. The study highlights the capability of the photogrammetry in aiding the structural analysis of imperfect engineering objects. Firstly, the photogrammetry measurements of a stiffened plate are carried out using a specially designed for the purpose experimental stand. Then, the plate surface geometry and structural configuration are reconstructed using commercial software. The resulting cloud of points is transformed into a regular mesh with a controlled grid size using a specially developed algorithm. The geometry of a stiffened plate, with measured initial imperfections, is then transferred to a finite element model and analysed. The ultimate strength analysis of stiffened plates considering different imperfections modelling techniques is conducted. The results are compared with the one obtained for measured imperfections, and several conclusions are derived. The proposed methodology revealed to be cost-effective and can be applied in various branches of shipbuilding and ocean engineering.

Keywords: Photogrammetry, Stiffened Plate, Ultimate Strength, FEM, Imperfections

1 Introduction

The steel structures are welded, which induces initial distortions and residual stresses in stiffened panels, affecting the structural behaviour and capacity. The welding-induced phenomena are complex and difficult to estimate during the design process. The effects of both residual stresses and distortions cause a reduction in load-carrying capacity of stiffened plates near the collapse load, smoothing the load-shortening curve in the relevant region (Gordo and Guedes Soares, 1993).

One of the first attempts to investigate the welding induced distortion and residual stresses was conducted by (Dow and Smith, 1984), who studied buckling and post-buckling behaviour of rectangular steel plates under compressive loads and concluded that the localised imperfection amplitude is one of the most important factors affecting the load-carrying capacity. Some other early studies related to this topic may be found in (Smith et al., 1988; Ueda and Yao, 1985), where the impact of initial distortions into the strength of plate elements has been studied. It was found that when the level of imperfections is significant, the strength of plates under uniaxial loads can be significantly reduced. The reduction was observed for plates with different levels of slenderness. The investigations of the impact of the initial imperfections into the ultimate capacity of other structural components were also carried out, including stiffened plates (Yu et al., 2019) and panels (Özgüç et al., 2007; Pedram and Khedmati, 2014) and the conclusions were similar. However, due to the existence of stiffeners, the

[1] Corresponding author e-mail: yordan.garbatov@tecnico.ulisboa.pt; Telf (351) 21 841 7907

reduction in the load carrying capacity was not significant compared to plates only. Some simplified methods for incorporating the initial imperfections influence in the ultimate strength predictions were proposed. Other experimental and numerical studies related to that problem may be found in (Chen and Soares, 2016; Manco et al., 2019).

Nowadays, the most commonly used method to predict the behaviour of thin-walled structures under compressive load is the non-linear finite element method; however, some closed-form solutions are useful too. There are various methods to take into account the initial imperfections. The first one is the implicit one; thus, some imperfections are taken into account during formula development, using rules and norms, such as the ultimate strength approach as stipulated by the Common Structural Rules (International Association of Classification Societies, 2018). The second method is to perform the linear buckling analysis firstly, and the shape of the first mode is to be used for the further non-linear calculation. The third method is applying some priorly assumed shape and level of the initial imperfections directly to the FE model. In the plates and stiffened plates, the commonly used method here is the Smith method (Smith, 1975). Finally, one can measure the actual value and shape of the initial imperfections of any particular structural element, employing various methods. The measurement of the initial imperfections is the essential work that needs to be done when evaluating the ultimate strength of different structural members experimentally. Furtherly, there need to be applied to the FE model.

Although photogrammetry originates mostly from the geodetic applications, founding a firm place in archaeological, paleontological and antique techniques. In terms of the latter, an extraordinary precision is required to preserve details for archiving or recovery purposes. (Lo Brutto and Spera, 2012) carried out a curious study, measuring a historic statue using two sister methods - photogrammetry (IBM - image-based) and laser scanning (RBM - range based). The study found that both methods produce similar detail and precision, with minor strengths and weaknesses over each other in several parts of the statue.

It should be noted that not all cameras are appropriate for performing photogrammetry measurements. Although it does not have to be a professional kit, at least a decent consumer-grade DSLR camera should be used. Still, a photogrammetric hardware kit is significantly cheaper than a laser scanner suitable for scanning large objects. It was shown by (Hellmuth et al., 2020) that even popular smartphone cameras have some success in measuring complex geometries, although limited by their insufficient optical capabilities.

Photogrammetry is not limited to large-scale objects. It copes well with small targets, and if executed properly - it can be even used for nano-scale metrology. In the study performed by (Gontard et al., 2016), a standard turntable image sequence is used to capture images of a single particle employing electron microscopy. The study transitions from multiple SEM images to a volume model and then to its 3D print representation in human scale. It is interesting to note that even though only recently such operations became technically accessible, the idea to reconstruct the 3D geometry from microscopic images is nearly as long-standing as digital imagery itself, as can be shown in (Crowther et al., 1970) (where the term “photogrammetry” is not even used) or (Piazzesi, 1973) (mathematical formulation). In (Garbatov et al., 2014), the photogrammetry has been employed to scan the corroded surface of small-scale fatigue specimens.

(Koelman, 2010) employed the photogrammetry to capture complete ship hulls for further analysis. It was noted that from an industrial point of view, the method was fairly simple and adequate while exhibiting numerous advantages over alternative methods. Inclusion of texture in the measured material, in addition to the standard geometry point cloud, was proven to be a major asset allowing

human-aided recognition of ship parts - a feature absent in akin laser scanning method. The other advantage is scale-independence of the photogrammetry, since capturing a larger object requires just taking more images or different scale images. Reaching for photogrammetry to measure initial imperfections of a modelled structure has been known for some time. It has been performed, e.g. in (Chen et al., 2011), where a structure was first measured, then modelled and both experimentally and numerically tested. The procedure included tedious marker placement and recognition designed to recreate structure deformation.

Marker placement is one of the core photogrammetry features, although it is not always necessary. In this study, we opted for markerless measurement to ensure that the original object surface is captured. In many applications, however, markers cannot be avoided. The most obvious purpose of using markers is model scaling, but there are others. It applies especially to the tasks, where several measurements of a single object are made over time, and they are later compared to compute the deformation of the object. Whether it is an evolution of the terrain surface in aerial photography with large markers (Hastaoğlu et al., 2019), displacements of a composite tank (Goda et al., 2019) or a strain field in a loaded steel plate (Li et al., 2014)- a set of markers (coded or not) is required to identify individual points in two compared models and compute the displacement field.

Nonetheless, these are advanced techniques, which bring photogrammetry close to DIC (Digital Image Correlation) systems in terms of automatic marker or pattern recognition and correlation. Generic photogrammetry often relies on surface measurement alone, such as in (Barbero-García et al., 2017) in a medical application (skull shape assessment). Even in this case, it was later supplemented with markers (Barbero-García et al., 2020) to track shape changes over time in the future.

In 3D geometry reconstruction tasks, a 3D surface model is usually sought as a final result. However, both the photogrammetry and the laser scanning produce unhampered 3D point clouds, which in principle do not form any specific surfaces. Surface generation is one of the geometry processing steps. Generic point clouds often include varying density and quality areas, resulting in uneven point distribution, out-of-plane points, and artefacts. It was noticed in (Armesto et al., 2009), who decided to manually mark characteristic points in a measured truss construction and used only these selected points as a wireframe geometry base for subsequent FE analysis. Pre-processing of point cloud with a resultant surface in mind is a tedious task, and algorithms supporting this process are still an open question. Efforts have been made to create universal tools for this task, such as edge-aware algorithm (Huang et al., 2013), or resampling method based on advanced mathematical tools (Chen et al., 2018). In this study, we also propose a numerical procedure, which - while simple - is specially designed for our measurement interests and works well for this case.

It can be noticed, that although the photogrammetry measurements were carried out for stiffened plates, there were rarely applied to the FE model to investigate the structural behaviour. Additionally, the presented approach is compared with the method that takes into account the assumed shape of initial imperfections, which is a commonly used methodology when considering numerical analysis.

2 Photogrammetry measurements

The analysed plates were of 1.265 m length, breadth 0.4 m with the flat bar stiffener of 0.1 m height. They were made from normal strength steel. The plates with stiffeners are with three different thicknesses: 5 mm, 6 mm and 8 mm. For each thickness, the four specimens were fabricated with the identical welding parameters. The specimens have been welded automatically, with the identical parameters of the welding process, which were monitored during welding.

A special experimental setup was prepared to perform the measurements of imperfections. Four cameras were attached to a frame, which was placed over a heavy steel table. The table was covered

with a dark blanket, and a measured specimen was lying on that blanket. During the measurement, a series of four images were taken simultaneously using a remote shutter, then the plate was slided to a next position (together with the blanket), and photos were taken. The process was repeated until the whole plate surface was captured in the images. The experimental rig was presented in Figure 1.

The approximate camera-to-object distance was 60 cm, while camera-to-camera distances were 32 cm for side pairs (1-2 and 3-4) and 48 cm for the middle 2-3 pair. The 1 and 4 cameras were pointed at the stiffener, while 2 and 3 cameras focused on the main plate surface. The change in position between subsequent slides was small enough to ensure a 50% overlap in neighbouring images.

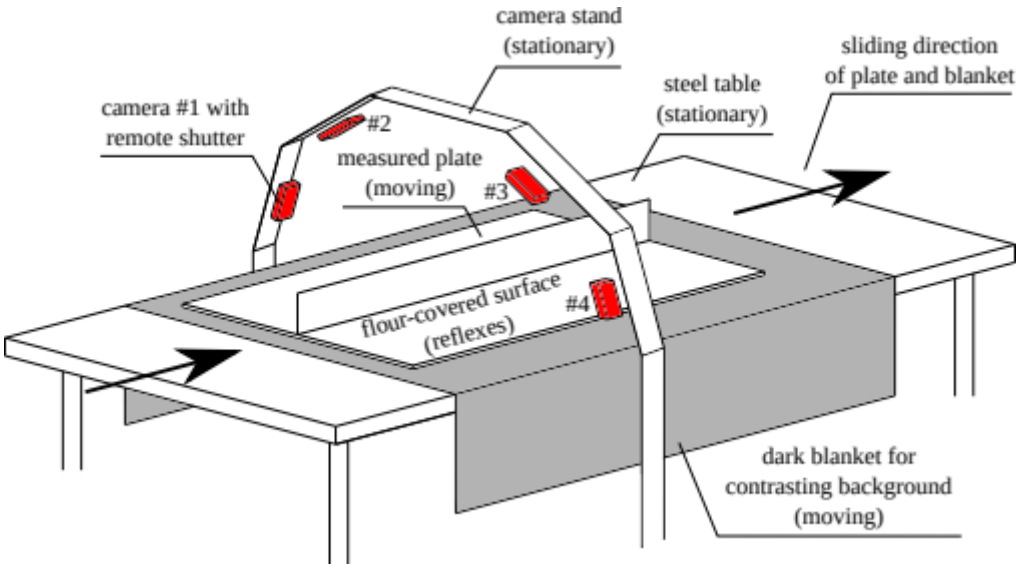

Figure 1. Draft of the experimental setup used for photogrammetric measurements.

The four cameras used for the measurement were Nikon D3300 equipped with Nikon AF-S DX VR Nikkor 18-55mm f/3.5-5.6G II interchangeable lenses. Nikon D3300 is a digital 24 MPx camera, capable of capturing 6000 x 4000 px images. All the images were taken with ISO sensitivity set to 100 (lowest possible on the used cameras), 18 mm focal length and f/3.5 aperture. Aperture priority settings with neutral exposure compensation were used. Shutter speed varied slightly between shots depending on the light distribution and camera location; however, it mostly revolved around 1/20s and rarely exceeded 1/10s. The aperture chosen was rather on the broadside; however, we decided to use it because of a) poor lighting conditions and lack of separate external lights (possible reflexes) and b) mostly perpendicular orientation of the measured surfaces concerning the lens optical axis. Admittedly, a narrower aperture and longer exposure time could have been used to improve the subsequent post-processing of the point cloud. All cameras were equipped with remote control shutters, which allowed the contactless and simultaneous acquisition of images. These traits are important for proper photogrammetry. Remote control eliminates unwanted vibrations of the camera rig caused by manual operation (even when the timer is utilised), while simultaneity speeds up the process by capturing a whole series at once instead of manipulating each camera separately. In the case of more unstable objects, it also ensures that the same moment and shape are captured in all the photos, but it is not that significant (examined plates are stiff and immobilised).

Real dimensions of the measured object need to be captured. To achieve this, scale bars or referencing markers are usually used. In our case, however, it was not advised, because surface topology was the essential part of capturing. Placing a scale bar or a marker on the object would alter (or overlay) its surface. Placing markers beyond the object was not an option, because the entire background was masked out later (required by the sliding method of acquiring successive image series). To overcome

these obstacles, markers (crosses) were drawn directly on the surface of the plates using a felt-tip pen (Fig. 4). Distances between the markers were measured in the real world and later introduced to the model during the post-processing stage. However, not the most precise, this approach allowed to capture the full original surface of the object. Because of space limitations and practical reasons, the camera rig was immobilised, and the plates were slided under the rig during image acquisition.

Figure 2. Example of image capture

An image capture example is shown in Figure 2 by the camera during the measurement. Steel reflexes were reduced by using potato flour since they have a negative impact on photogrammetric measurements results (Agisoft LL, 2020). In the corners of the plate, there are white cross markers. The distance between the markers along the plate was measured and then used to scale the photogrammetric model.

The majority of image processing was executed in two software pieces: Agisoft Metashape (Agisoft LL, 2020), a commercial package for photogrammetry, and RawTherapee (The RawTherapee Team, 2020), an open-source image-editing software. Original images are taken in a Nikon-owned raw NEF format. Agisoft PhotoScan requires prior conversion to JPG or TIFF format, with the latter lossless format preferred. Conversion from NEF to TIFF was performed using RawTherapee software. It is important to note that the default Neutral profile includes automatically applied lens correction based on the EXIF data. Default settings apply only basic radial barrel/pincushion compensation. Agisoft PhotoScan manual states that any image manipulation is undesirable at this stage, so it was decided to leave the photos originally distorted as in RAW files.

Each photo includes some part of a measured object and background - partially static (camera stand, room), partially not (dark blanket). Since in each photograph, the measured plate changes its position, but the background also evolved (contrasting blanket), it was necessary to perform the walk-around masking scenario and not the more specific turntable scenario (which is possible in the case of a completely static background). A relevant object area was selected in each photo, and the rest masked out, including out-of-focus object surfaces, edges, and background (irrelevant). In-focus areas were identified mostly visually.

During the camera alignment phase, relative positions of cameras are calculated, and a sparse point cloud of the measured object is created (Fig. 3). Camera alignment was then optimised to ensure that these points overlap in respective projection planes. We used High settings, which means that full-resolution photos have been used to perform camera alignment and build the initial sparse point cloud. Masked-out areas were excluded from the process.

Figure 3 shows the Initial sparse point cloud and estimated positions of cameras after performing the camera alignment step. In the back, yellow lines represent camera-to-camera distances. Each set of 4 photos was taken in a different position and time.

After the sparse cloud is created, the dense cloud is built based on the aligned cameras projections. This cloud requires some manual cleaning (out of plane points, artefacts, choppy edges, etc.). Basing on the dense cloud, a surface is created, consisting of triangular mesh elements. The aggressive depth

filtering was chosen during the surface generation, which means that a smooth, continuous surface was desired.

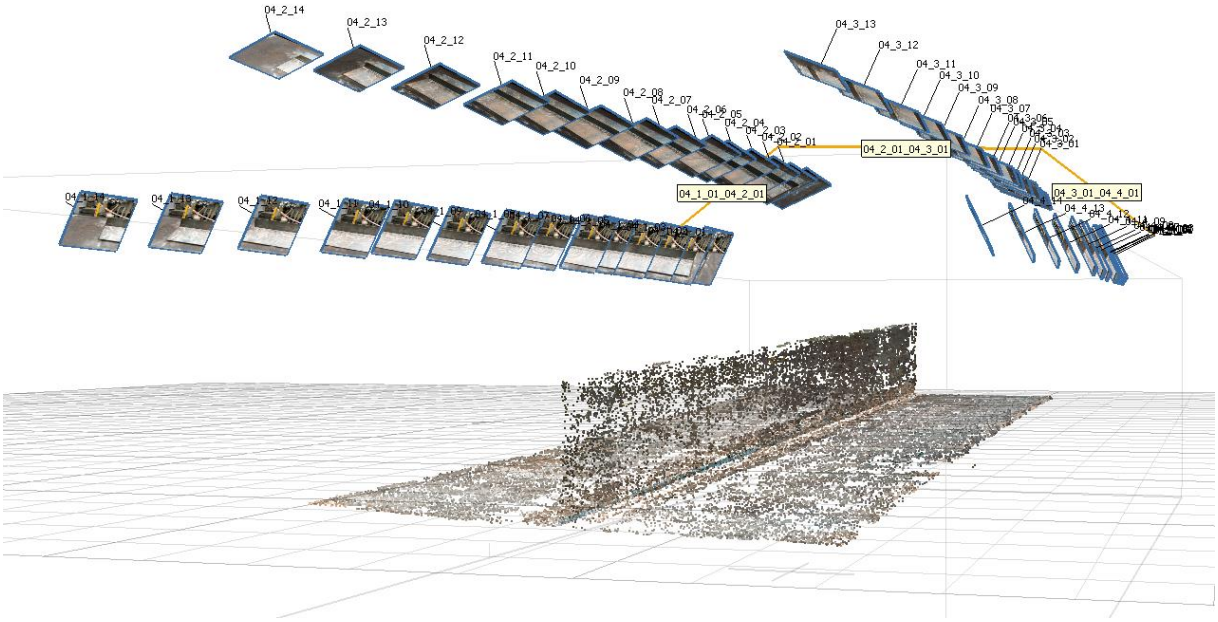

Figure 3. Initial sparse point cloud and estimated positions of cameras

The final step of photogrammetric reconstruction was texturing of the surface. Here we can choose between the Mosaic mode (only the sharpest photos representing given area are used for texturing) or the Average mode (all photos covering a given area are used). The average mode was selected because it provides precious information about consistency - if some textured area appears blurred, it means that it was reconstructed based on images of variable quality. It may be an indicator of a potential problem with precision in this area. This information is absent in the Mosaic mode, which selects only the best photographs for texturing. In our study, all the textures were consistently sharp, which allowed us to identify their features without problems.

Because using scale bars, markers, or reference points was not possible; we decided to pre-calibrate the camera rig using a chequerboard calibration plate as described earlier. For each experimental setup, an initial photogrammetric reconstruction of chequerboard was performed. A coordinate system was set to align with the plate edges, and a scaling factor was set to ensure the proper size of the model. Coordinates of a specific camera rig position were then exported. These coordinates were planned to be used later in photogrammetric models of measured plates; however, it turned out to be unnecessary - the distance between the white cross markers provided sufficient precision of global plate dimensions. Fig. 4 shows the textured photogrammetric model with the white cross markers included and used as scale bars. Two scale bars (along each long edge) were used, and the variance between them was computed. It turned out to be negligible, so no additional scaling methods were utilised).

The entire software processing time, including image preparation, masking (manual work), dense cloud generation, export and resampling, took about 1 hour per specimen. The computer used for this task was equipped with 32 GB RAM, Intel i7-8700 3.2 GHz 6 core CPU and Nvidia Quadro P4000 8 GB DDR5 GPU.

Figure 4. Textured photogrammetric model.

3 Analysis of initial imperfections

The geometrical model created in Agisoft Metashape can be exported, whether as point cloud coordinates or an STL surface. These models are usually not directly appropriate for FE analysis because of their excessive size and numerous inconsistencies. It is possible to use a built-in downsampling procedure to reduce the size of the model, but the outcome also lacks quality. An example result of such operation has been presented in Figure 5. We can see that although the point cloud is visibly sparser, the nodal lines are not aligned along the plate edges. There are numerous discontinuities and shifts in the grid order.

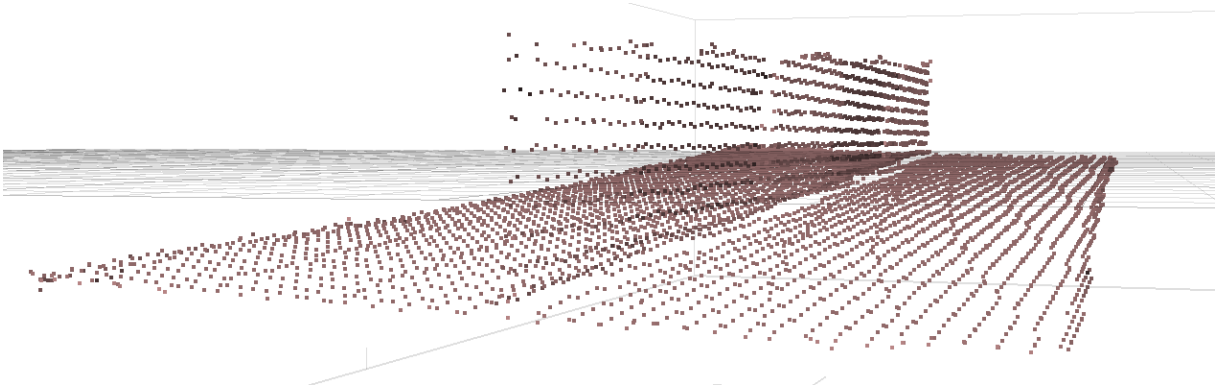

Figure 5. Built-in Agisoft Metashape downsamples procedure.

Figure 5 shows the built-in Agisoft Metashape downsamples procedure. At the same time, the density of the point cloud is visibly reduced. It can be seen that the node lines are not parallel to the plate edges and are partly non-continuous. This point cloud is not suitable for direct use as a FEM mesh node-set.

To overcome these obstacles, an algorithm in Matlab (Mathworks, 2019) is used in creating organised nodal lines, while representing global imperfections and preserving local imperfections of the measured plates. Automation was required since we had to prepare 14 geometrical models - each in different mesh size variants - for FE analysis. For this purpose, we started with importing the dense point cloud and getting rid of the edges, which - being boundary areas - are the most prone for reconstruction error (Fig. 6). The main plate and the stiffener are also separated at this stage and are processed individually in all subsequent steps.

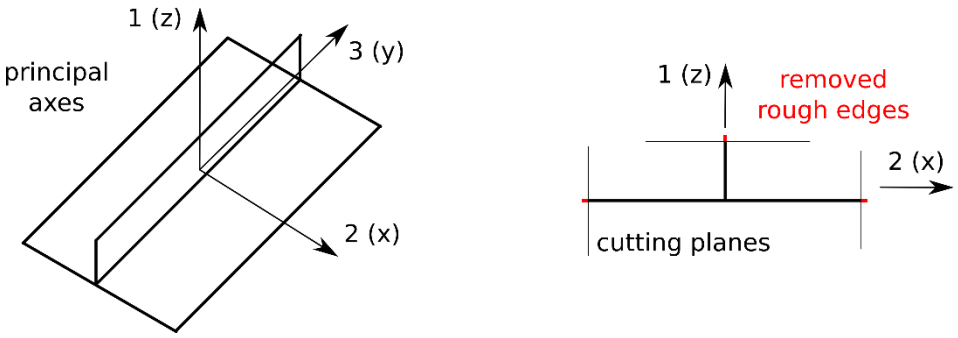

Figure 6. Computed principal axes of inertia for plate orientation (left) and trimmed rough edges providing smooth surface (right).

Because of the natural flaws of edges representation (masking artefacts, diffraction, etc.), see Figure 6, the point cloud was trimmed to enhance later automation of mesh generation. Each plate specimen had its principal axes of inertia computed and used to achieve optimal cutting planes orientation. This approach allowed an automated preparation of data without manual supervision of the process.

Afterwards, the mesh grid lines were created, and each point from a point cloud was assigned to a field isolated by the grid lines. In each isolated field, a centre of mass was calculated, and a best-fit-plane was found based on the distribution of imported points (Fig. 7). A normal vector of this plane represented the local tilt of a measured specimen in two directions. As an effect, each field of the mesh grid was equipped with a centre of mass (elevation-wise) and a corresponding normal vector representing the distribution of the point cloud in this field. A general plane equation:

$$ax + by + cz + d = 0 \tag{1}$$

including $[abc]$ components of the normal vector is used. Eqn (1) can be simplified, assuming that the component *c* of the normal vector is 1. This assumption can be made, because the plane orientation is almost horizontal in all cases, resulting in a nearly vertical normal vector. The plane is only slightly tilted (imperfections). Thus $a$and $b$components are small in comparison to c. Only the vertical (z −axis) component of a node-to-plane distance is taken into consideration this way, but it leads to a relatively small error while linearising the problem at the same time. Finally, the plane equation is represented as:

$$ax + by + d = -z \tag{2}$$

and the a, b, dcomponents can be found using the relation:

$$\begin{bmatrix} x_0 & y_0 & 1 \\ x_1 & y_1 & 1 \\ \dots & x_n & \end{bmatrix} \begin{bmatrix} a \\ b \\ d \end{bmatrix} = \begin{bmatrix} -z_0 \\ -z_1 \\ \dots \\ -z_n \end{bmatrix} \tag{3}$$

where n is the total number of points in a given isolated field, and $[xyz]$are the respective coordinates of these points. The final normal vector can be obtained by normalisation of the $[ab1]$ vector so that the earlier assumption of $c = 1$is neglected (a normal vector's magnitude needs to be 1). A normal vector of a plane is found in a single step, which satisfies the condition that the vertical z component of total node-to-plane distance is minimised. Figure 7 shows the method used in computing normal

vectors of isolated areas (groups of points isolated by grid lines from the point cloud) and elevations of corner nodes.

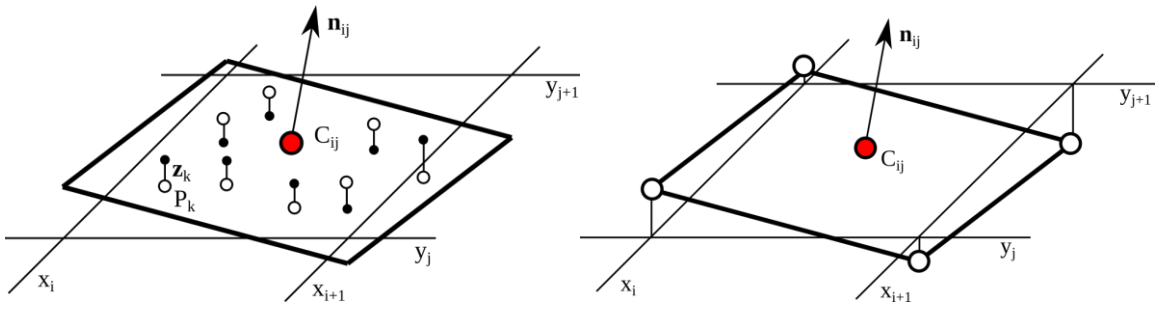

Figure 7.Computing normal vectors of isolated areas

Based on the centre-normal pairs, coordinates of the corner nodes positioned along the grid lines can be calculated. Since most target mesh nodes (except for the plate edges) are common for the four neighbouring element corners, their elevations are averaged from all the neighbours (Fig. 8). This way, it is possible to preserve a smooth, continuous character of the surface while including the originally measured imperfect features of the specimen.

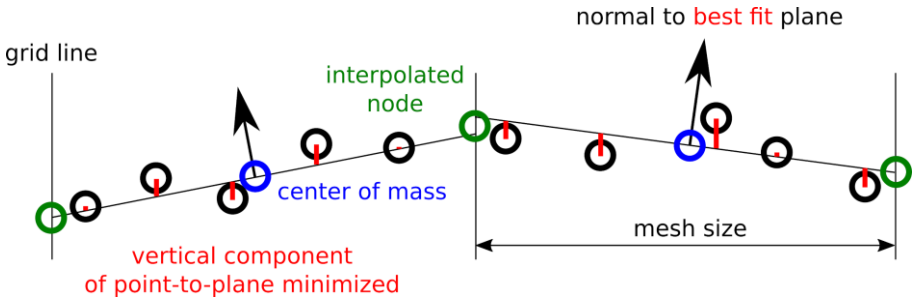

Figure 8. Grid nodes (green) are interpolated from corner nodes of all adjacent areas (2D view).

As a final result of the procedure, a well-organised node-set is created, closely representing the measured plate dimensions. In our case, two separate meshes are generated - one for the main plate, the other one for the stiffener. They are tied together in the central axis. An example of such a process has been presented in Figure 9. The measured imperfections (two opposite bulges) are easily noticeable.

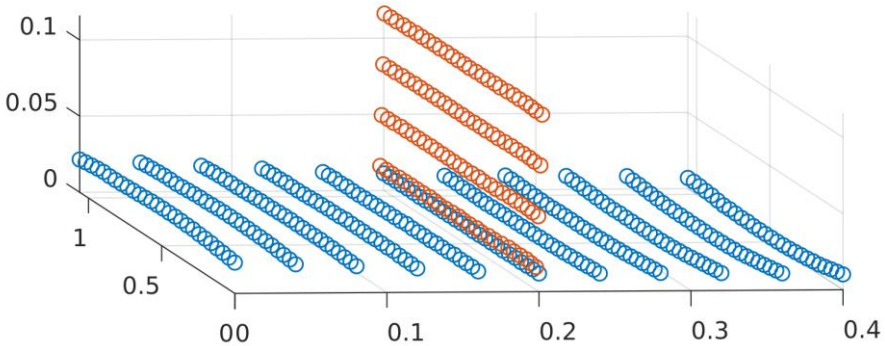

Figure 9. Outcome of organised downsampling procedure.

Based on the measurements one can indicate the common shape of initial plate imperfections, where the stiffener imperfections are denoted as c_0. Where the positive sign is in the b_1 and b_2 imperfections, the shape is similar to the one presented in Figure 10. The minus sign denotes that curvature of imperfection is the opposite.

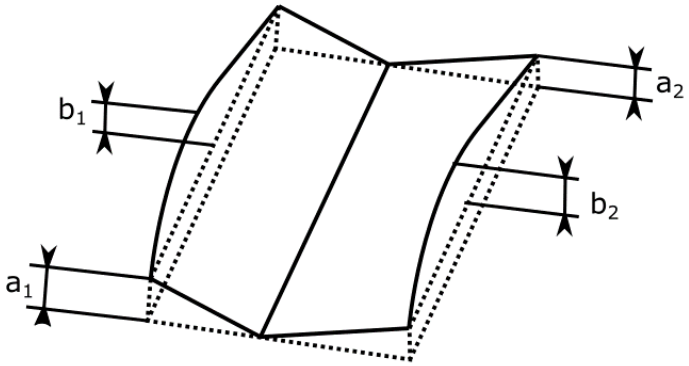

Figure 10. Initial imperfections.

The values for initial imperfections are presented in Table 1.

Table 1. Imperfections measurements.

Plate thickness	No	a_1 [mm]	a_2 [mm]	b_1 [mm]	b_2 [mm]	c_0 [mm]
5 mm	1	2.37	5.19	-7.98	5.37	1.19
	2	3.45	3.05	-8.91	9.02	3.35
	3	2.78	3.37	-6.98	4.49	2.95
	4	2.33	3.49	-5.34	3.95	0.00
	Mean	2.73	3.77	-7.30	5.71	1.87
6 mm	1	3.73	3.66	3.69	-4.10	2.18
	2	4.01	4.17	3.58	-4.95	0.72
	3	4.62	3.12	2.19	-5.01	0.85
	4	4.36	3.21	0.63	-5.19	0.60
	Mean	4.18	3.54	2.52	-4.81	1.09
8 mm	1	3.77	5.50	-3.01	-2.43	0.22
	2	4.31	5.07	-0.25	-0.11	0.44
	3	4.25	4.73	1.39	1.46	0.77
	4	6.13	4.88	-2.16	-3.21	0.37
	Mean	4.61	5.05	-1.01	-1.07	0.45

The shape of the initial imperfections is consistent with other literature examples (Garbatov et al., 2016). One can notice that when the plate is thicker, the general sideways imperfections are bigger (a_1, a_2), whereas the local plate imperfections are tend to be smaller (b_1, b_2). Similarly, the stiffener imperfections are smaller, with the increase of plate thickness. In the case of 5 mm and 6 mm plates, the local plate imperfections are of the opposite signs in both sides of the stiffener. In the case of 8 mm plate, the plate imperfections are of the same sign. It is also notable, that although the welding conditions were the same for each thickness of stiffened plates, the imperfections are subjected to considerable scatter. However, a trend of mean values evolution along the changes in thickness is sustained, leading to the conclusion that the measurements reflect the general condition of the plates.

The typical shapes of initial imperfections for different thicknesses of stiffened plates are presented in Figure 11. One can notice that with the increase of the plate thickness, the global imperfections are more dominant, whereas the local imperfections are less significant.

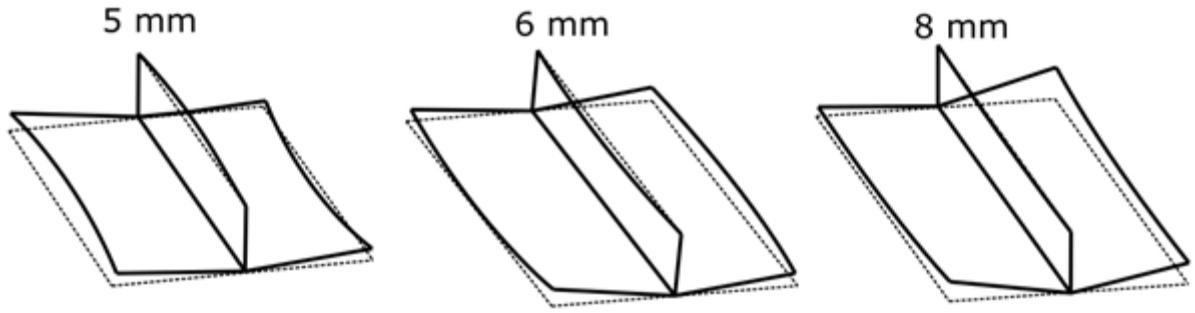

Figure 11. Initial imperfections of specimens (scale factor 5x).

4 FE analysis

Commercial software (ANSYS, 2019) is used to generate finite element models. The non-linear static solver employing the Arc-length method is used to obtain the load-carrying capacity of any particular studied case. The four-node SHELL181 elements are used to model both plate and stiffener. There are two types of nonlinearities considered here: material nonlinearity (material is considered a bilinear one) and geometric nonlinearity (large deformations).

The boundary conditions are modelled as fixed ones on the shorter edges and free on the longer edges (see Figure 12). The stiffened plates are subjected to a displacement-driven load to obtain the force-displacement curve for each case and resulting in the ultimate strength. The initial imperfections are based on the photogrammetry measurements, and there are implemented by changing the z-coordinate of each finite element node.

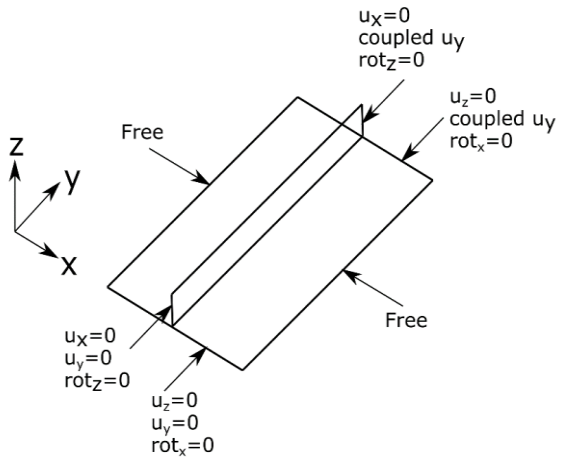

Figure 12. Applied boundary conditions.

To obtain the best possible results, the mesh convergence study has been performed. The studied mesh sizes were in the range from 0.01 m up to 0.04 m. It has been determined that the mesh size of 0.02 m lead to an accurate value of ultimate strength and providing relatively low computational time.

The mechanical properties are based on the tensile testing of the coupon specimens. The mean values for each thickness are presented in Table 2. The material model is considered as bilinear with hardening.

Table 2. Material properties of considered steel plates.

Thickness [mm]	Yield stress [MPa]	Young modulus [GPa]	Ultimate tensile stress [MPa]	Total elongation [-]
5	263.2	199.0	386.5	0.278
6	279.3	190.6	404.8	0.267
8	357.5	196.7	457.0	0.224

5 Results

The post-collapse shapes of 5 mm specimens are presented in Figure 13. In all cases, the post-collapse is caused by local plate buckling followed by stiffener tripping. Nevertheless, the post-collapse shapes differ between each specimen, resulting from differences in initial imperfections distributions. The cross-section position, which is subjected to the highest plastic deformations varies between specimens. In the case of specimen 5.2, it is even very close to the support. This indicates that the imperfections are different in terms of the maximum values as presented in Table 1 and has different distributions along with the specimens.

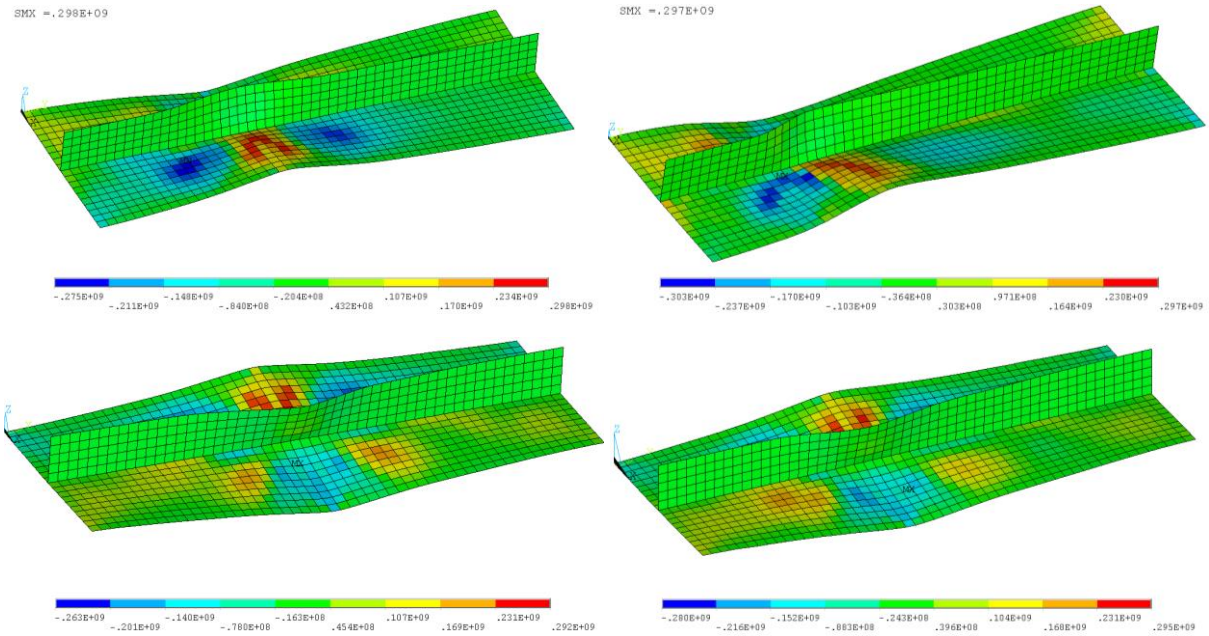

Figure 13. Post-collapse form of deformation in model with real imperfections – 5mm plates (5.1 -left up, 5.2 – right up, 5.3 – left bottom, 5.4 – right bottom). Normal stresses (longitudinal direction) distribution in Pa.

The differences in force-displacement curves between specimens are noted too (see Figure 14), especially in the post-collapse behaviour. The ultimate force varies between 399.8 kN for 5.1 specimens up to 403.9 kN for 5.2 specimens, so the impact of differences in imperfections on that value is not significant (about 1 % of difference). The initial inclinations of the force-displacement curves are different and the specimen with the highest value of local imperfections (b_1, b_2) shows the

lowest rigidity. In opposite, the most rigid is specimen 5.4, which has the lowest initial local imperfections. Further, for a specimen of the highest initial imperfections, the displacement where maximum force is reached is higher than other specimens. Additionally, for that case, the collapse is not so rapid leading to more smooth force-displacement curve in the region of maximum compressive force. In all cases, there is no explicitly visible bifurcation point, where initial buckling occurred.

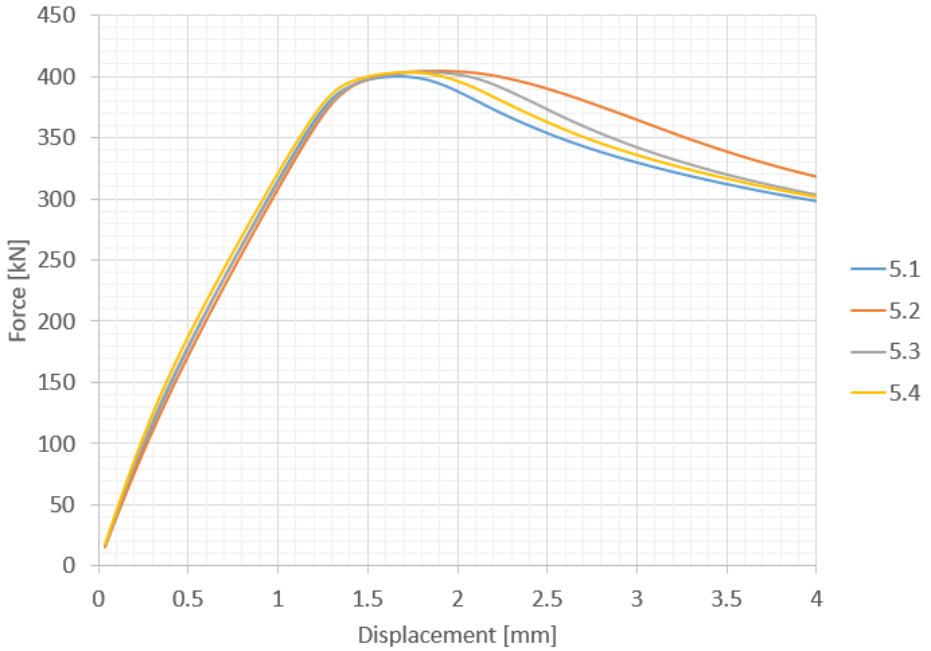

Figure 14. Force-displacement curves for 5 mm specimens.

The post-collapse shapes for 6 mm specimens are presented in Figure 15. The failure mode is plate buckling followed by stiffener tripping. Similarly to 5 mm specimens, the post-collapse shapes differ between each other. In each case, the position where maximum deflections after the collapse occurred is different. Additionally, in the case of 6.2 specimens, the plate collapsed very near the support leading to different shape of the collapsed plate and stiffener.

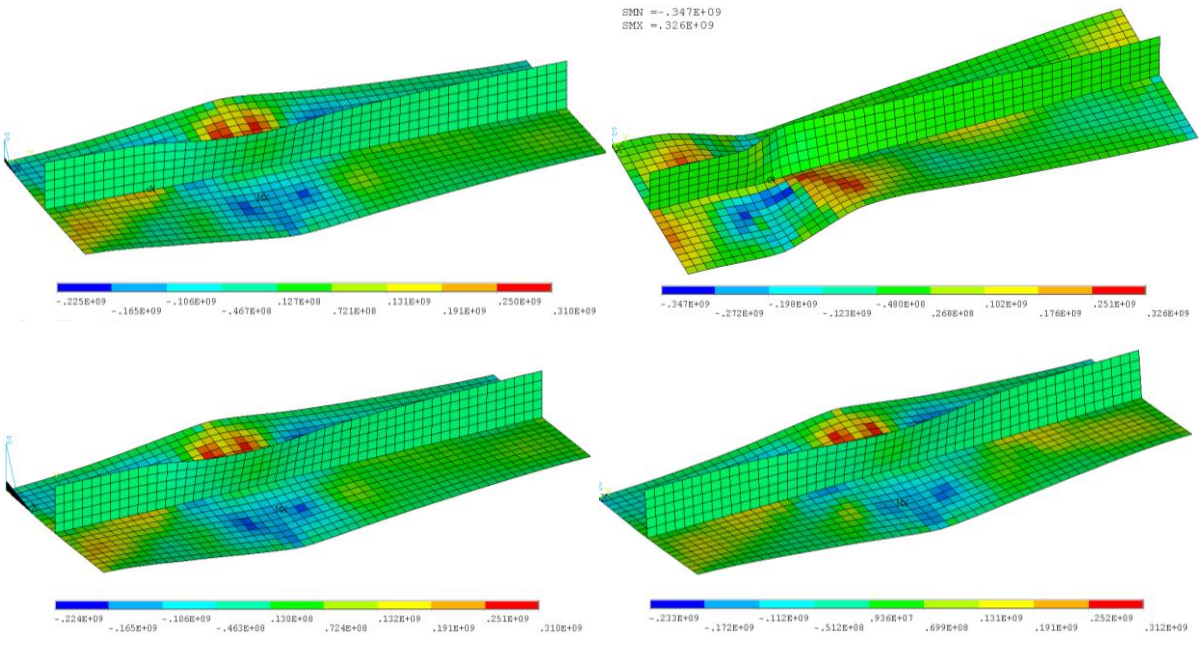

Figure 15. Post-collapse form of deformation in model with real imperfections – 6 mm plates (6.1 - left up, 6.2 – right up, 6.3 – left bottom, 6.4 – right bottom). Normal stresses (longitudinal direction) distribution in Pa.

In the case of force-displacement curves for 6 mm specimens (see Figure 16), the differences can also be visible. The ultimate force is between 535.9 kN and 538.5 kN. The specimen with the lowest local imperfections (6.4) has the biggest rigidity in the beginning and curve deviate concerning other ones. However, in this case, the deviations are smaller with compared to 5 mm plates. In the case of post-collapse behaviour, only 6.2 specimen deviates from others. This is connected with different post-collapse shape observed for this specimen concerning others, as shown in Figure 15. It could be concluded that these deviations are originated from different initial imperfections distributions in the specimens, although the maximum values are rather similar. Similarly to 5 mm specimens, the explicit bifurcation point cannot be traced.

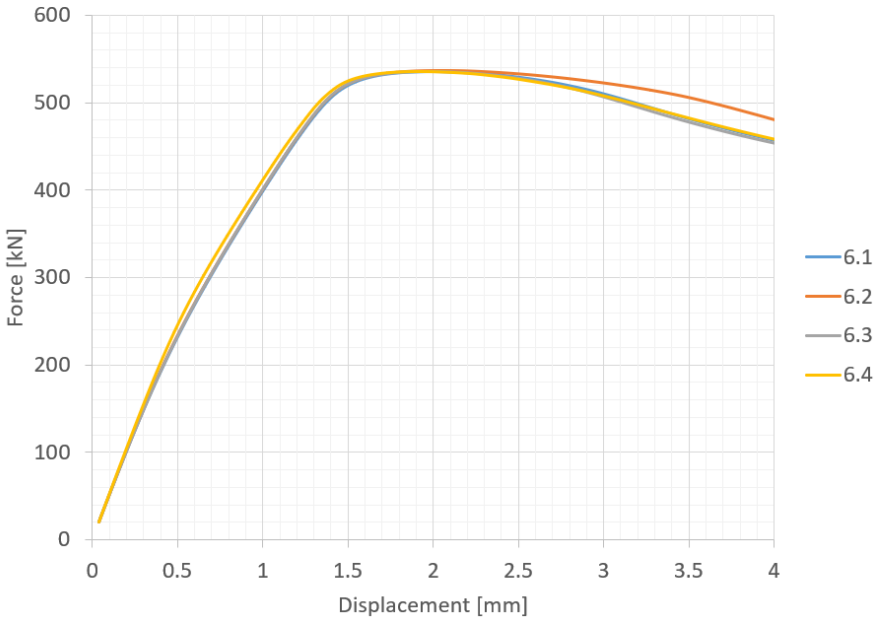

Figure 16. Force-displacement curves for 6 mm specimens.

The post-collapse forms of 8 mm specimens are presented in Figure 17. Based on the stress distributions, it could be noticed that in this case, the failure mode was a combination of local plate buckling and global column buckling. In that case, the post-collapse shapes are not differing much between the specimens. In all cases, the maximum plastic deflections occurred very close to the middle cross-section.

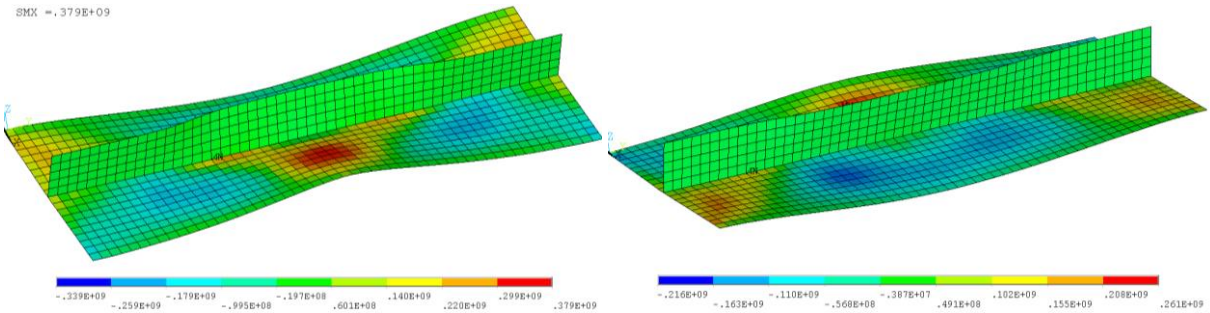

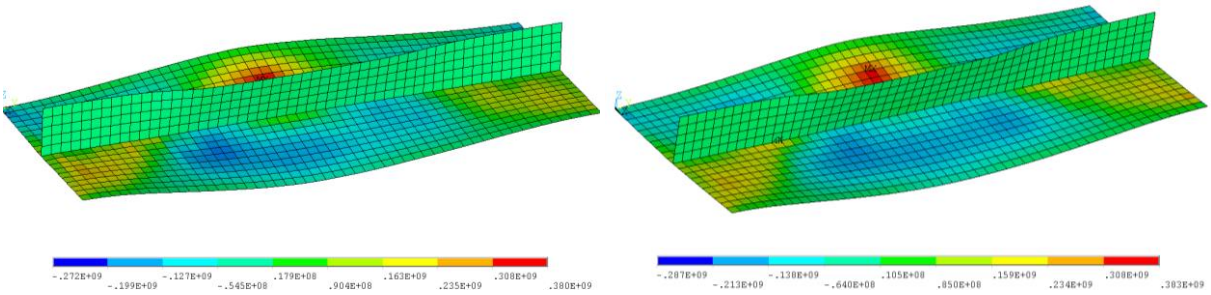

Figure 17. Post-collapse form of deformation in model with real imperfections – 8 mm plates (8.1 - left up, 8.2 – right up, 8.3 – left bottom, 8.4 – right bottom). Normal stresses (longitudinal direction) distribution in Pa.

The force-displacement curves for 8 mm specimens are presented in Figure 18. Similarly to post-collapse shapes, the force-displacement curves are not deviating between specimens much. However, in that case, the bifurcation point is observed, and some deviations in that region could be observed. The most explicitly visible for 8.2 specimens is the lowest local initial imperfections (only 0.25 mm and 0.11 mm). It is known that when imperfections are lower, the buckling behaviour is more rapid, and the bifurcation point is explicitly visible.

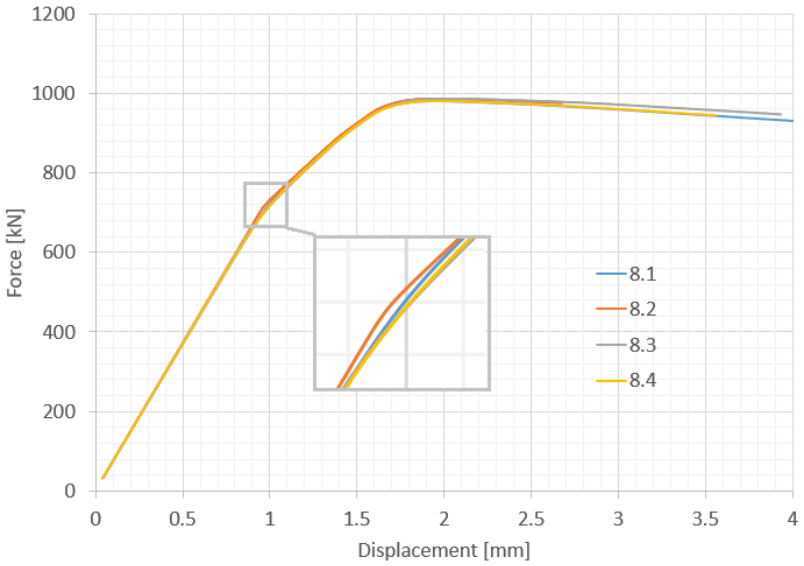

Figure 18. Force-displacement curves for 8 mm specimens.

In general, the differences in initial imperfections has a low impact on the value of the ultimate force. In the case of post-collapse shape, the differences are noted for thinner plates (5 mm, 6 mm), whereas for thicker plates the shapes are very similar. The similar observation could be noted by comparison of force-displacement curves.

The differences in places of maximum plastic deformations between the specimens indicate that the imperfections vary in terms of maximum value and the distributions along with the specimen. In case of 5 mm and 6 mm specimens, the initial local imperfections with opposite signs of both side of stiffener lead to collapse without clearly visible bifurcation point, since the collapsed form was similar to the initial shape of specimens. In the case of thinner 5/6 mm plates, both the deflection and the stress distribution have more of a local, concentrated character. Changes in deformation and stress are rapid and dramatic. Thicker plates manage to resist deplanation using its full length and width. The stress distribution is much milder, and the areas near supports are also affected. This phenomenon is

not noticeable using artificially generated imperfections, which is discussed later in the text. The support area is nearly untouched by stress, which is concentrated mostly in the middle part of the plate regardless of its thickness.

6 Comparison with other initial imperfections modelling techniques

When the initial imperfections are not known, one needs to assume their value and shape. Based on the study of (Smith, 1975), the initial imperfections of the stiffened plate can be modelled as presented in Figure 19, where the imperfections are the superposition of global distortions in longitudinal direction modelled as a half-sin wave with c_0 level and local plate distortions with the level of δ_0 and modeled as a half-sin wave in both longitudinal and transverse direction.

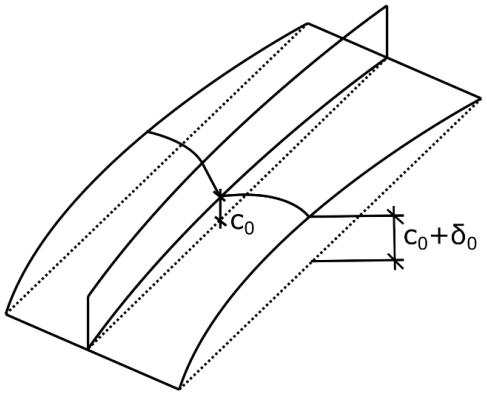

Figure 19. The initial imperfections modelled using Smith approach.

The level of initial imperfections can be calculated based on the plate slenderness ratio β:

$$\beta = \frac{b}{t}\left(\frac{\Re}{E}\right)^{0,5} \tag{4}$$

where E is the elastic modulus, $\Re$ is the yield stress, b is the plate breadth and, t is the plate thickness.

The maximum value of plate imperfections can be calculated as follows:

$$\frac{\delta_o}{t} = 0.1\beta^2 \tag{5}$$

The longitudinal imperfection of the stiffened plate, $\frac{c_0}{l}$ is as well as stiffener imperfections can be considered equal to:

$$\frac{c_0}{l} = 0.0015 \tag{6}$$

Using the following model, the specimens with three different thicknesses are analysed, leading to post-collapse shapes, as presented in Figure 20. From the beginning, one can notice, that in the case of the assumed shape of initial imperfections, the collapsed form is symmetrical with regards to middle cross-section and maximum deflections occur in that place. In case of plates with real imperfections, the usually non-symmetrical collapse was observed due to unsymmetrical distribution of initial imperfections. In case of failure modes, for plates with the assumed shape of imperfections, a local plate buckling is followed by stiffener tripping. In the case of plates with real imperfections, the similar

modes are observed in 5 mm and 6 mm plates. However, for 8 mm plate, the failure mode is rather the combination of local plate buckling and global column buckling. This could also be noticed when looking at stress distributions. In the case of 8 mm plate with real imperfections, both compressive and tensile zone are quite extended along the plate length (see Figure 20) and in case of Smith approach, these zones are localised in the middle of the specimen rather limited extension.

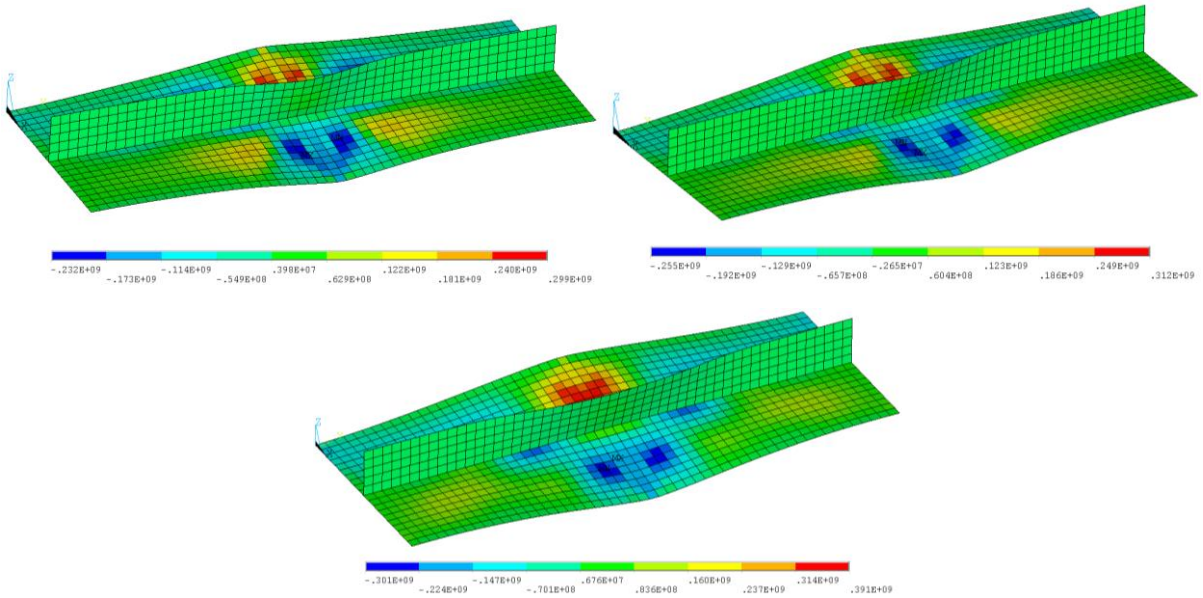

Figure 20. Post collapse shapes for imperfections based on smith approach (5 mm plate –left up, 6 mm plate – right up, 8 mm plate – bottom). Normal stresses (longitudinal direction) distribution in Pa.

Due to the differences in the yield stresses due to different plate thicknesses, the normalised stress – mean strain curves are introduced instead of force-displacement curves. The stress is divided by material yield stress on the vertical axis, whereas, on the horizontal axis, the longitudinal displacement divided by plate length is presented. The comparison between mean response for stiffened plates with real measured imperfections and following the Smith approach is presented in Figure 21. It could be noticed that the differences are quite significant in the case of 5 mm and 6 mm plates. Firstly, in both cases, the explicit bifurcation point is noted for plates with artificial imperfections, which could not be traced for plates with the measured imperfections. In the case of the measured imperfections, the collapsed shape was closer to the initial shape of the specimens; thus, the buckling was not so dramatic.

Additionally, the initial inclination of the stress-strain curve is significantly higher for the first case. Further, the point of the ultimate capacity is reached with smaller strain in plates analysed with artificial imperfections and collapse is more rapid. In plates with real imperfections, the region of maximum stress is quite wide, and collapse is less rapid. With regards to the 8 mm plate, both curves are rather similar. The initial inclinations are almost the same leading to bifurcation point, which occurs for slightly higher stress in case of artificial imperfections. The ultimate point cover in both curves and post-collapse behaviours are rather the same.

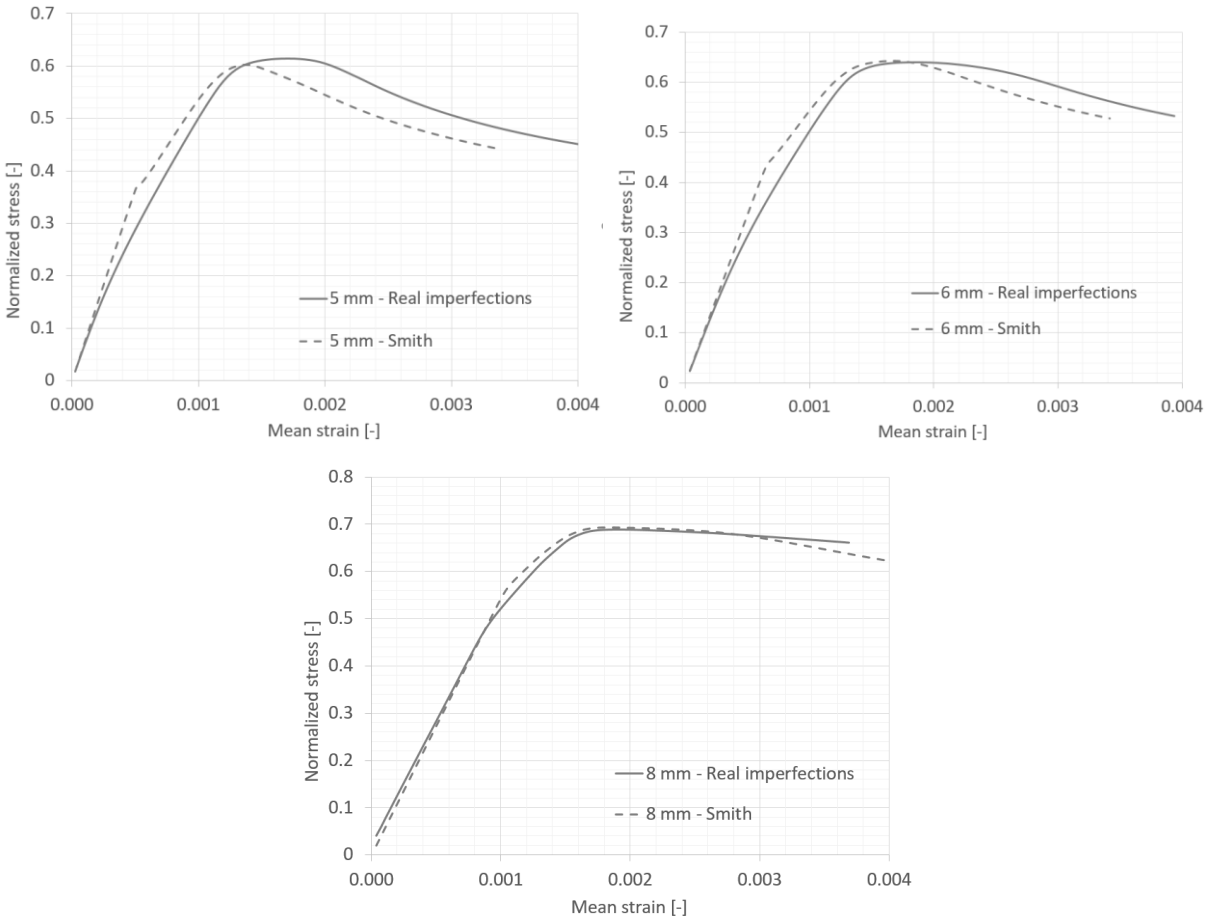

Figure 21. Sress-strain curves for specimens with real initial and generated initial imperfection.

Finally, the values of normalised ultimate stress are compared in Table 3. It could be observed that there are no notable differences between ultimate stress values. In the case of 5 mm plate, the capacity is slightly higher in real imperfections, whereas for 6 mm and 8 mm plates, it is the opposite.

Table 3. Results of normalised ultimate stress.

Thickness [mm]	Normalised ultimate stress [-]		Difference [%]
	Real imperfections – mean value	Artificial imperfections	
5	0.612	0.603	1.56
6	0.640	0.643	-0.47
8	0.687	0.694	-0.98

7 Conclusions

The approach presented in this work for imperfect structural modelling employed a photogrammetry image-based technique and FE non-linear analysis. The tool revealed to be swift and easily applicable due to its multiple assets. Firstly, the methodology avoids using the special markers and image-based point-cloud resampling is performed with the specially developed code. Thus, it can be easily applied to analyse the strength behaviour of an existing structure, especially when harsh in-situ conditions

exist. Secondly, the proposed approach shows that the initial imperfections measurement via photogrammetry technique is very efficient in further processing as input for the FE analysis.

However, it should be noted that this approach can not be used to accurately compare two measured states (e.g. initial and deformed), since physical markers are lacking and identification of individual points (nodes) is hindered. Displacement and strain fields are not to be captured this way. Markerless approach with automatic mesh generation is well-suited for - and excels in - acquiring accurate geometry for further FE analysis. One large advantage of this method is scale independence - it can be applied to an object of any size. However, the object and the scene require some preparation. In large reflecting surfaces, such as ship hulls, chalk paint can be used to obtain a matte finish. This approach has been already tested with success by the authors in another, yet unpublished study.

It has been observed, that apart the identical welding parameters were provided for each specimen, the imperfections varied between each other, leading to differences in both post-collapse shapes and force-displacement responses. The differences are more significant in the thinner plate. This could be related to the increasing plate slenderness ratio, and for higher values of that parameter, the structural behaviour is more sensitive with regards to the initial imperfections level. Employing the real imperfections bring more variance to the deformation and stress distribution of different plate thickness. Although the ultimate force is hardly affected, the qualitative difference is easily noticeable to the eye. However, using different welding parameters, the differences in load-carrying capacity could be significantly higher too.

Comparing the proposed approach with the commonly used methodology of a priorly assumed shape and level of initial imperfections revealed some differences. Primary, the assumed shape of imperfections led to a symmetrical post-collapse shape of each specimen, which has not been observed for real imperfections, due to uneven distribution. In the case of the Smith approach, the buckling has been more dramatic and explicit bifurcation point has been noted, and post-collapse behaviour has been more rapid.

The presented numerical approach with the application of measured initial imperfections has also been validated against experiment in (Woloszyk et al., 2020), showing a good convergence in terms of both values of ultimate strength and the post-collapse behaviour of the specimens.

The developed approach is highly recommended to assess the residual structural capacity of ageing structures and that subjected grounding and collision, where the real deflections can be measured and analysed. Employing the developed approach, based on the assessed maximum capacity of the structure, an acceptable level of the structural imperfection for any specific structural component and environment of operation may be derived. This cost-effective measurement and processing method can also be used to assess the geometrical accuracy of manufactured objects against their design, such as plane plate control in the shipyard. The proposed methodology could also be utilised in the so-called ‘reverse engineering’, such as the renovation of historical boats.

Acknowledgements

The National Science Centre, Poland has supported this work (grant No. 2018/31/N/ST8/02380). The ANSYS software used in presented simulations in this paper was available as a part of the partnership cooperation agreement between ANSYS Inc., MESco sp. z o.o., and the Gdansk University of Technology. Agisoft Metashape Professional Educational License software provided by the Gdansk University of Technology was used for photogrammetric purposes. Part of the calculations was carried out at the Academic Computer Centre in Gdańsk.

Disclosure statement

No potential conflict of interest was reported by the authors.

References

Agisoft LL, 2020. Agisoft Metashape User Manual: Professional Edition.

ANSYS, 2019. Online Manuals, Release 19.

Armesto, J., Lubowiecka, I., Ordóñez, C., Rial, F.I., 2009. FEM modelling of structures based on close-range digital photogrammetry. Autom. Constr. 18, 559–569. https://doi.org/10.1016/j.autcon.2008.11.006

Barbero-García, I., Lerma, J.L., Marqués-Mateu, Á., Miranda, P., 2017. Low-Cost Smartphone-Based Photogrammetry for the Analysis of Cranial Deformation in Infants. World Neurosurg. 102, 545–554. https://doi.org/10.1016/j.wneu.2017.03.015

Barbero-García, I., Lerma, J.L., Mora-Navarro, G., 2020. Fully automatic smartphone-based photogrammetric 3D modelling of infant's heads for cranial deformation analysis. ISPRS J. Photogramm. Remote Sens. 166, 268–277. https://doi.org/10.1016/j.isprsjprs.2020.06.013

Chen, B.-Q., Guedes Soares, C., 2016. Deformation measurements in welded plates based on close-range photogrammetry. Proc. Inst. Mech. Eng. Part B J. Eng. Manuf. 230, 662–674. https://doi.org/10.1177/0954405414558734

Chen, B.Q., Garbatov, Y., Guedes Soares, C., 2011. Measurement of weld-induced deformations in three-dimensional structures based on photogrammetry technique. J. Sh. Prod. 27, 51–62.

Chen, S., Tian, D., Feng, C., Vetro, A., Kovacevic, J., 2018. Fast Resampling of Three-Dimensional Point Clouds via Graphs. IEEE Trans. Signal Process. 66, 666–681. https://doi.org/10.1109/TSP.2017.2771730

Crowther, R.A., DeRosier, D.J., Klug, A., 1970. The reconstruction of a three-dimensional structure from projections and its application to electron microscopy. Proc. R. Soc. London. A. Math. Phys. Sci. 317, 319–340. https://doi.org/10.1098/rspa.1970.0119

Dow, R.S., Smith, C.S., 1984. Effects of localised imperfections on compressive strength of long rectangular plates. J. Constr. Steel Res. 4, 51–76. https://doi.org/10.1016/0143-974X(84)90035-X

Garbatov, Y., Guedes Soares, C., Masubuchi, K., 2016. Residual Stresses and Distortion in Welds, in: Reference Module in Materials Science and Materials Engineering. Elsevier. https://doi.org/10.1016/B978-0-12-803581-8.03036-8

Garbatov, Y., Guedes Soares, C., Parunov, J., 2014. Fatigue strength experiments of corroded small scale steel specimens. Int. J. Fatigue 59, 137–144. https://doi.org/10.1016/j.ijfatigue.2013.09.005

Goda, I., L'Hostis, G., Guerlain, P., 2019. In-situ non-contact 3D optical deformation measurement of large capacity composite tank based on close-range photogrammetry. Opt. Lasers Eng. 119, 37–55. https://doi.org/10.1016/j.optlaseng.2019.02.006

Gontard, L.C., Schierholz, R., Yu, S., Cintas, J., Dunin-Borkowski, R.E., 2016. Photogrammetry of the three-dimensional shape and texture of a nano-scale particle using scanning electron microscopy and free software. Ultramicroscopy 169, 80–88. https://doi.org/10.1016/j.ultramic.2016.07.006

Gordo, J.M., Guedes Soares, C., 1993. Approximate Load Shortening Curves for Stiffened Plates Under Uniaxial Compression. Proc. Integr. Offshore Struct. - 5. https://doi.org/10.13140/RG.2.1.3643.2801

Hastaoğlu, K.Ö., Gül, Y., Poyraz, F., Kara, B.C., 2019. Monitoring 3D areal displacements by a new methodology and software using UAV photogrammetry. Int. J. Appl. Earth Obs. Geoinf. 83, 101916. https://doi.org/10.1016/j.jag.2019.101916

Hellmuth, R., Wehner, F., Giannakidis, A., 2020. Datasets of captured images of three different devices for photogrammetry calculation comparison and integration into a laser-scan point cloud of a built environment. Data Br. 33, 106321. https://doi.org/10.1016/j.dib.2020.106321

Huang, H., Wu, S., Gong, M., Cohen-Or, D., Ascher, U., Zhang, H. (Richard), 2013. Edge-aware point set resampling. ACM Trans. Graph. 32, 1–12. https://doi.org/10.1145/2421636.2421645

International Association of Classification Societies, 2018. Common Structural Rules (BC & OT).

Koelman, H.J., 2010. Application of a photogrammetry-based system to measure and re-engineer ship hulls and ship parts: An industrial practices-based report. Comput. Des. 42, 731–743. https://doi.org/10.1016/j.cad.2010.02.005

Li, L.-G., Liang, J., Shi, B.-Q., Guo, C., Hu, H., 2014. Grid-based photogrammetry system for large scale sheet metal strain measurement. Optik (Stuttg). 125, 5508–5514. https://doi.org/10.1016/j.ijleo.2014.06.069

Lo Brutto, M., Spera, M.G., 2012. Image-based and range-based 3D modelling of archaeological, cultural heritage: the Telamon of the Temple of Olympian Zeus in Agrigento (Italy). ISPRS - Int. Arch. Photogramm. Remote Sens. Spat. Inf. Sci. XXXVIII–5, 515–522. https://doi.org/10.5194/isprsarchives-XXXVIII-5-W16-515-2011

Manco, M.R., Vaz, M.A., Cyrino, J.C.R., Ramos, N.M., Liang, D.A., 2019. Experimental and numerical study of uniaxially compressed stiffened plates with different plating thickness. Thin-Walled Struct. 145, 106422. https://doi.org/10.1016/j.tws.2019.106422

Mathworks, 2019. Matlab R2019b.

Özgüç, Ö., Das, P.K., Barltrop, N., 2007. The new simple design equations for the ultimate compressive strength of imperfect stiffened plates. Ocean Eng. 34, 970–986. https://doi.org/10.1016/j.oceaneng.2006.05.013

Pedram, M., Khedmati, M.R., 2014. The effect of welding on the strength of aluminium stiffened plates subject to combined uniaxial compression and lateral pressure. Int. J. Nav. Archit. Ocean Eng. 6, 39–59. https://doi.org/10.2478/IJNAOE-2013-0162

Piazzesi, G., 1973. Photogrammetry with the scanning electron microscope. J. Phys. E. 6,

392–396. https://doi.org/10.1088/0022-3735/6/4/023

Smith, C., 1975. Compressive strength of welded steel ship grillages. Trans RINA 118, 325–359.

Smith, C., Davidson, P., Chapman, J., Dowling, P., 1988. Strength and Stiffness of Ships' Plating under In-plane Compression and Tension. Trans. RINA 130.

The RawTherapee Team, 2020. RawTherapee.

Ueda, Y., Yao, T., 1985. The influence of complex initial deflection modes on the behaviour and ultimate strength of rectangular plates in compression. J. Constr. Steel Res. 5, 265–302. https://doi.org/10.1016/0143-974X(85)90024-0

Woloszyk, K., Garbatov, Y., Kowalski, J., Samson, L., 2020. Experimental and numerical investigations of ultimate strength of imperfect stiffened plates of different slenderness. Polish Marit. Res. 27, 120–129.

Yu, Y., Feng, G., Li, C., Ren, H., 2019. Experimental and Numerical Investigation on the Ultimate Strength of Stiffened Plates with Scanned Initial Geometrical Imperfection. China Ocean Eng. 33, 446–458. https://doi.org/10.1007/s13344-019-0042-4